Chemical interaction between uranium dioxide, boron carbide and stainless steel at 1900°C – Application to a severe accident scenario in Sodium cooled Fast Reactors

Mathieu Garrigue[a*], Andrea Quaini[a], Thiery Alpettaz[a], Christophe Bonnet[a], Emmanuelle Brackx[b], Renaud Domenger[b], Matthieu Touzin[c], Olivier Tougait[d], Christine Guéneau[a]

[a] Université Paris-Saclay, CEA, Service de la Corrosion et du Comportement des Matériaux dans leur Environnement, 91191, Gif-sur-Yvette, France

[b] The French Alternative Energies and Atomic Energy Commission, Bagnols sur Cèze, Languedoc-Roussillon, France

[c] Univ. Lille, CNRS, INRAE, Centrale Lille, UMR 8207 - UMET - Unité Matériaux et Transformations, F-59000 Lille, France

[d] Univ. Lille, CNRS, Centrale Lille, ENSCL, Univ. Artois, UMR 8181 - UCCS - Unité de Catalyse et Chimie du Solide, F-59000, Lille, France

* Corresponding author: Mathieu Garrigue

Highlights:

- The interaction between UO_2 and a mixture (B_4C + stainless steel) at 1900°C leads to the two-phase equilibrium: UO_{2-x} + liquid
- The liquid phase contains stainless steel components, bore and about 4-5 at% of uranium
- Thermodynamic calculations confirm that a carbo-reduction reaction with CO(g) formation occurs between UO_2 and C from the liquid phase

- Several mixed boride phases containing mainly Fe, Cr and to a lesser extent U, form during solidification. Ni is mainly located in intermetallic compounds containing U and Fe
- Absorber element B may chemically bound fuel elements U

Abstract:

For the understanding of severe accidents in sodium cooled fast reactors (SFR), it is necessary to understand two prototypic accident scenarios such as ULOF (Unprotected Loss of Flow Accident) and UTOP (Unprotected Transient OverPower). As the base knowledge, it is also important to understand high temperature chemical interaction among major core materials such as MOx fuel (MOx: mixed oxide of uranium and plutonium), steel cladding and B_4C neutron absorber have to be investigated. This study aims at providing experimental data on phase formation and phase-stability at various temperature and pressure conditions. A first series of samples containing a mixture of B_4C and steel were prepared to obtain a homogenous metallic solid. In a second step, these metallic samples were mixed and melted with small UO_2 pieces by arc melting. Then these samples underwent a heat treatment at 1900°C for 1 hour. EDS, EBSD and EPMA analyses were performed to identify the phases formed during the solidification. In addition, thermodynamic calculations were performed for the interpretation of the results, revealing that a carbo-reduction reaction occurs: $UO_2 + 2\ C = 2\ CO + U$. A significant amount of uranium from the fuel is dissolved in the metallic liquid phase, leading to the formation of mixed borides (UM_3B_2, UMB_4, UM_4B, M=Fe,Cr,Ni). In comparison with the UO_2/steel interaction, the present results show that the presence of B and C in the melt improves the wetting behaviour of the metallic liquid towards UO_2.

Keywords: severe accident, sodium fast reactor, B_4C, carbo-reduction, UO_2, stainless steel,

Glossary:

BSE: Back Scattered Electron

EBSD: Electron Backscatter Diffraction

EDS: Energy Dispersive Spectroscopy

EPMA: Electron Probe Microanalysis

SEM: Scanning Electron Microscopy

SFR: Sodium Fast Reactor

SS: Stainless Steel

TAF-ID: Thermodynamic Advanced Fuel – International Database

ULOF: Unprotected Loss of Flow

UTOP: Unprotected Transient OverPower

1. Introduction

In the framework of safety analysis for sodium cooled fast reactor (SFR), severe accidents associated to a core meltdown are investigated. Calculation codes, such as SIMMER [1,2] or EUROPLEXUS [3], are used to simulate fluid-dynamics and structure damages of reactor core during severe accident. These codes do not take into account the complex thermochemistry of core materials yet. The purpose of this study is to investigate the high temperature thermo-chemical behaviour of a typical SFR core materials during a severe accident.

In the SFR reactor, the fuel pellets are stacked in 15-15-Ti stainless steel (SS) cladding (named AIM1) [4]. B_4C is the standard neutron absorber used in control rods. B_4C rods are cladded with SS. In case reactivity increases, the fuel temperature may rise up to the SS melting. Several scenarios can lead to the partial or full fuel melting. This work focuses on chemical reactions occurring during a specific core meltdown accident, Unprotected Transient

Over-Power (UTOP) or Unprotected Loss Of Flow (ULOF). In those scenario, the reactor core integrity is engaged [5,6]; the formation of a complex solid-liquid core materials mixture may occur from the chemical reaction between the fuel, stainless steel and B_4C. In UTOP, withdrawal of control rod leads to local temperature increase. Extreme temperatures might even lead to fuel assembly melting [7] and fuel ejections out of pins [5,8–10]. Large pool of biphasic liquid (metallic and oxide) may form and extend. In ULOF, loss of cooling efficiency initiates generalized core degradation and melting [5]. In both case, to reduce the fuel reactivity, safety procedures require dropping B_4C control rods into the degraded core. Indeed, keeping B_4C and fuel mixed helps containing reactivity. .

Temperature may reach SS melting point in seconds or minutes depending on cores and scenarios [2]. In the standard design of control rods, a SS cladding surrounds B_4C material. An eutectic reaction at 1200°C [11–14] may lead to a B_4C/SS liquid formation. Therefore, in the case of temperature escalation, the SS (from both fuel pin cladding and absorber cladding) may melt and lead to liquid state interactions with the surrounding materials [15],with in a first step, the B_4C/SS interaction.

In this work, interaction tests were performed between molten mixtures of SS/B_4C and UO_2 samples. An annealing was performed at 1900°C for 1 hour to attempt approaching ULOF conditions. Then the fast-cooled samples have been characterized using SEM (scanning electron microscopy) and EDS (Energy Dispersive Spectroscopy), EPMA (Electron Probe Microanalysis) and EBSD (Electron Backscatter Diffraction) to analyse the phase chemical compositions and structures. Finally thermodynamic calculations were performed with the version 11 of the TAF-ID [16] (Thermodynamic Advanced Fuel – International Database) to explain the experimental results. The test targets enhancing core materials understanding at high temperature. The study of solidified phases aims to interpret high temperature interactions and at identifying chemical behaviour of B and U elements during core materials

cooling down. In a broader perspective, the study of solidified phases is part of a large thermodynamic modelling project that contributes to improve modelling of solid-state complex systems.

2. Experimental procedure

2.1.Sample preparation

B_4C pieces, AIM1 SS chips and depleted UO_2 pellet fragments were used as starting materials for samples preparation. B_4C pieces were obtained from hollow hexagonal blocks designed for nuclear reactors use. AIM1 SS was chosen as pin cladding material because AIM1 constitutes the major part of SS in SFR cores [17,18]. UO_2 was chosen as fuel simulant because of its major influence to MOx fuel behaviour and its ease of handling. The compositions of those starting materials are reported in Table 1.

Table 1 Raw materials composition in mass%.

	U	O	B	C	Fe	Cr	Ni	Mo	Ti	Balance
UO_2	88.04	11.96	-	-	-	-	-	-	-	-
B_4C	-	-	78.35	21.65	-	-	-	-	-	-
Stainless steel	-	-	-	0.08	66.18	14.29	15.06	1.50	0.39	2.50

Sample compositions (Table 2) corresponds to prototypic conditions. They were chosen to match relevant range for ULOF. To mimic as close as possible accident conditions where a molten mixture of SS/B_4C is in contact with the fuel, B_4C and SS were first melted using an arc melting furnace. Then a second arc-melting was performed to get a good contact between the SS/B_4C mixture and the UO_2 pellet. Three samples were made following this procedure. B_4C and UO_2 are refractory materials tricky to arc-melt so consequent mass losses were measured after melting. In each case, the mass loss does not exceed 5% of the total mass after successive melts. The large masse losses of sample n°1 outcomes from a UO_2 pellet fracture

during arc melting. This tiny loss of few mg of UO_2 compared to the starting mass is considered as negligible on the thermodynamic equilibrium. Initial raw material masses and respective mass losses are presented in Table 2 for each sample.

Table 2 Samples compositions in mg

Sample	UO_2 (mg)	B_4C (mg)	SS (mg)	Weight percentage UO_2-B_4C-SS	Total weight loss during arc melting (mg)
Sample n°1	341.6 ± 0.1	71.3 ± 0.1	568.4 ± 0.1	35 – 7 – 58	49.4 ± 0.1
Sample n°2	168.5 ± 0.1	33.1 ± 0.1	279.4 ± 0.1	35 – 7 – 58	8.2 ± 0.1
Sample n°3	300.3 ± 0.1	36.3 ± 0.1	306.2 ± 0.1	47 – 6 – 47	1.0 ± 0.1

2.2.Experimental setup

The sample n°1 is chosen as reference to check the impact of the heat treatment on the two remaining samples, namely samples n°2 and n°3. Therefore, sample n°1 did not undergo any heat treatment. Sample n°1 and n°2 have the same composition. In sample n°3, only the UO_2 amount was increased in order to study the influence of an increasing content of this component on the reaction. The samples labelled n°2 and n°3 were heated in the same batch. Annealing was performed in a tungsten furnace at 1900°C for 1 hour under vacuum ($7x10^{-8}$ mbar). The samples were then cooled at an average rate of 60°C/min, the fastest cooling rate allowed by the setup. Further details about the experimental method are available in previous work by Quaini et al [19].

To minimise interaction between samples and W-crucibles, a specific setup has been designed (Figure 1). A small Y_2O_{3-x} crucible (CEA supply) was placed into a screwed tungsten crucible (Plansee supply). The samples were placed into the Y_2O_{3-x} crucible to protect the W crucibles and the furnace.

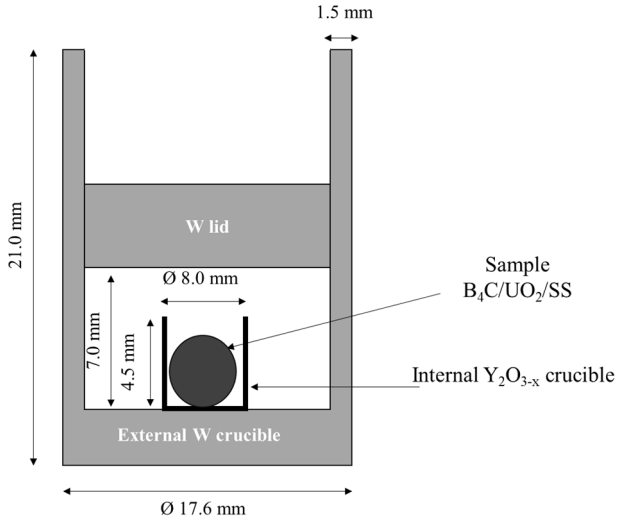

Figure 1 Layout of the crucible setup used during the heat treatment

Following heat treatment, the samples were cut and polished to observe the cross-sections by using SEM. Quantitative determinations of the phase compositions and structure-types were performed by Energy Dispersion Spectroscopy (EDS), Electron Back-Scattered Diffraction (EBSD) and Electron Probe Micro-Analyser (EPMA). SEM-EDS measurements were performed using a ZEISS MERLIN microscope with an EDS Oxford Instruments X-Max 80mm detector. EBSD measurements were performed in a ZEISS SUPRA microscope with e-flash Brucker HR+ detector and on a HITACHI SU5000 microscope equipped with an Oxford Instruments Symmetry detector. EPMA analysis were done in a CAMECA SX100 microscope. Standards used for EPMA calibration are listed in Table 3.

Table 3 Standards used for EPMA calibration.

Element	U	O	B	C	Fe	Cr	Ni
Standard	UO_2	UO_2	B	TiC	Fe	Cr	Ni
Element	Mo	Ti	Mn	Si	Y	W	
standard	Mo	Ti	Mn	$Ca_3Fe_2Si_3O_{12}$ (Andratite)	Y	W	

2.3.Thermodynamic calculations

To understand and interpret the experimental results, thermodynamic equilibrium calculations were performed using the Thermo-calc software and the version 11 of the TAF-ID [16] database. The TAF-ID database contains reliable models for the fuel and structural material and therefore is suitable to investigate the UO_2-B_4C-SS system at high temperature. In this work, calculations aim at evaluating the composition of the phases in equilibrium at 1900°C. Thermodynamic calculations were then compared to the experimental results. This approach helped both in expounding the experimental results and in testing the reliability of the version 11 of the TAF-ID database.

3. Results

In this section, the samples microstructure and the phases compositions are discussed based on EDS, EBSD and EPMA measurements. SEM cross-section images of sample n°1, n°2 and n°3 are shown in Figure 2.

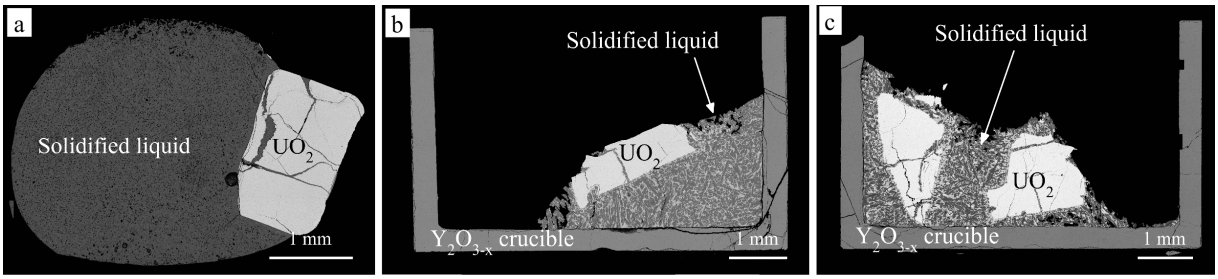

Figure 2 Back-scattering electron image of sample cross-sections: a) Sample n°1 – b) Sample n°2 – c) Sample n°3

3.1. Sample n°1

This reference sample did not undergo any heat treatment, allowing the comparison with the annealed samples. Figure 3 shows the microstructure of the solidified B_4C/SS liquid in contact with the UO_2 pellet after arc melting and the corresponding BSE micrographs and EBSD phase map. The Figure 3a shows a good wetting behaviour of the B_4C/SS liquid

mixture on the UO_2 surface, in contrast with observations on liquid SS and UO_2 [20,21]. An overall composition measurement on the solidified liquid area using EPMA indicates the presence of Fe, Cr, Ni, B and C (Table 4). Only traces of uranium, shaped as thin acicular phase, are visible from BSE chemical contrast. The total amount of U in the solidified liquid phase is below the detection limit of both EDS and EPMA analyses. No oxygen was found in the solidified liquid. The large amount of C measured in EPMA is irrelevant considering the initial composition. The excess may result from external contamination and should not be interpreted as quantitative result. The absence of uranium and oxygen shows that there was no significant interaction between the metallic melt and UO_2. Compositions of all the phases are reported in Table 5, while the Figure 3 labels them over BSE and EBDS pictures.

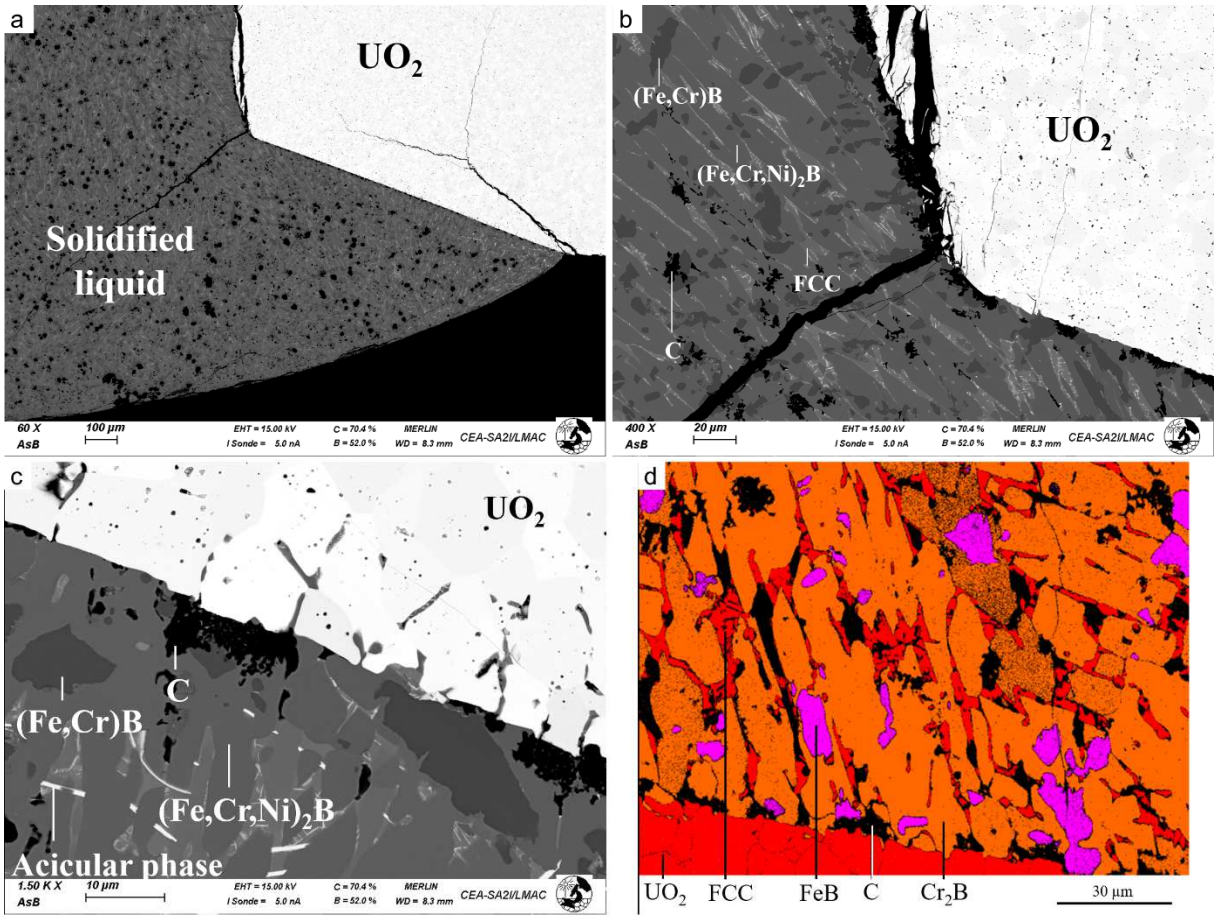

Figure 3 SEM images of sample n°1 – a) BSE image zoom x60 – b) BSE image zoom x400 – c) BSE image zoom x1500 – d) EBSD map zoom x800. C does not diffract in EBSD. The labbel is arbitrary added according to its specific microstructure.

Five phases are observed in the solidified liquid region:

- The tetragonal boride $(Fe,Cr,Ni)_2B$ with I4/mcm space group and Al_2Cu-type (Pearson Symbol: *tI*12). It is the major phase;
- The orthorhombic boride (Fe,Cr)B with Pnma space group and FeB-type (Pearson Symbol: *oP*8) with dendritic shape (always surrounded by $(Fe,Cr,Ni)_2B$ phase);
- The cubic metallic phase diffracting as *fcc* structure enriched in Fe and Ni;
- An acicular phase with unidentified crystallographic structure dispersed into the *fcc* phase;
- C-Graphite precipitates.

Phase compositions and crystal structures identified in this work are similar to those observed in different studies about SS-B_4C interactions (Takano et al.[22], Sumita et al.[15], Aizenshtein et al. [23]), with the exception of a different structure-type assignment for (Fe,Cr)B phase which is found as adopting the FeB-type structure instead of the CrB-type.[22]. The dissimilar Cr concentration in SS and the B_4C/SS ratio might explain this difference between both studies. Similarly to Takano et al. [22], graphite precipitates with small boron content were observed (the B/C ratio measured by EPMA is about 0.3).

3.2.Sample n°2

Figure 4 shows the microstructure of the solidified molten B_4C/SS mixture in interaction with the UO_2 pellet in sample n°2.

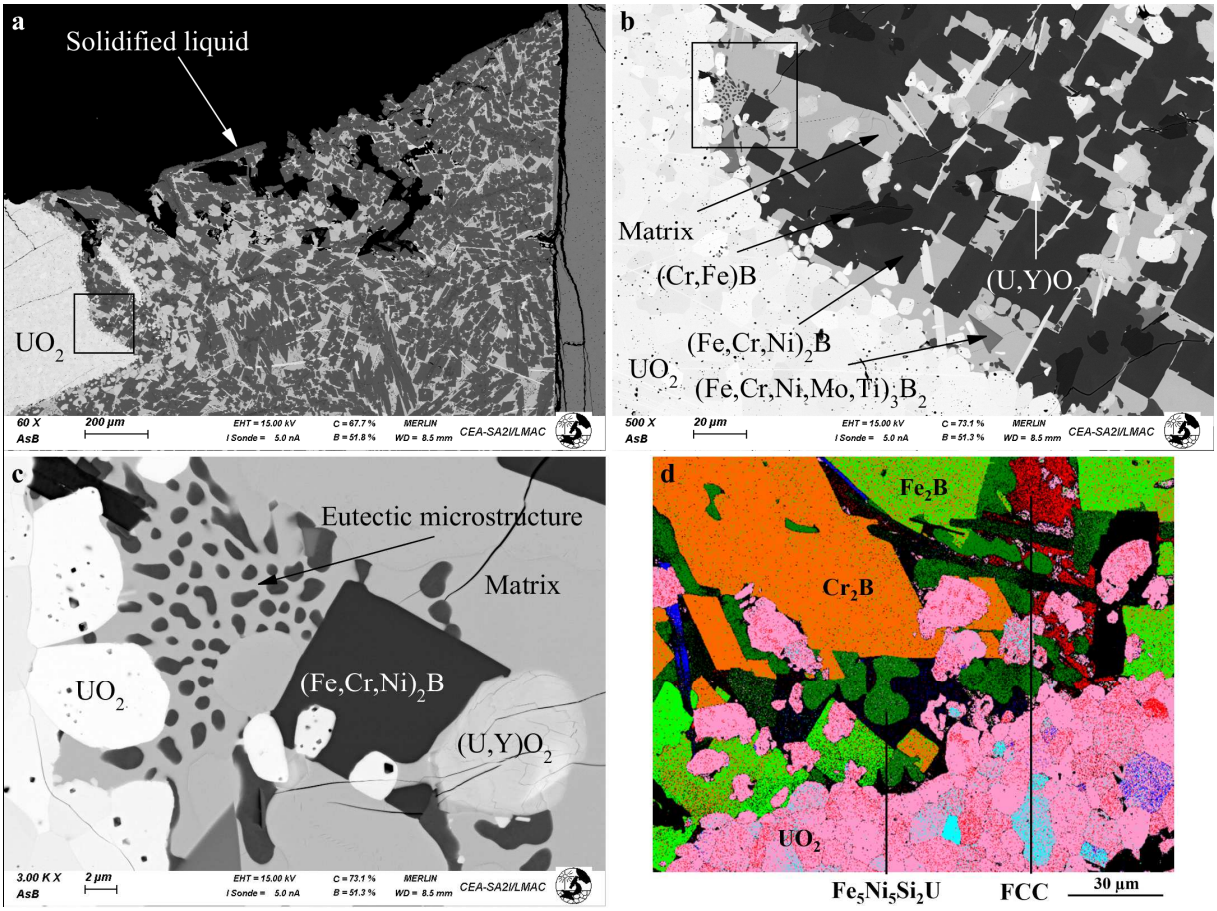

Figure 4 SEM images of sample n°2 – a) BSE image zoom x60, black square indicates the location of the top right picture – b) BSE image zoom x500, black square indicates the location of the bottom left picture – c) BSE image of eutectic area, zoom x3000 – d) EBSD map zoom x700, legend corresponds to the indexed structures as compound-like notation. Light blue and purple are residual indexations of insignificant *fcc* phases, they belong to the UO_2 phase.

The solidified liquid phase has a homogenous microstructure and uniformly wets the entire UO_2 pellet chip. An intergranular penetration of the liquid at the UO_2 interface is observed. The observed intergranular penetration of the liquid may have promoted the mechanically removal of UO_2 grains. Some local eutectic microstructures are observed (Figure 4c). Overall composition measurements by EPMA indicate that the solidified liquid mainly contains Fe, Cr, Ni, B and U (Table 4). C remains below the detection limit. Only traces of C are found in

boride phases. Thus, the global C-content is negligible. Phase compositions and crystal structures were identified by coupling EPMA and EBSD measurements (Table 5).

In total ten phases were observed (Figure 4). First, the UO_2 phase of the unreacted pellet diffracting as *fcc* phase according to EBSD. EPMA measurements corroborate these EBSD results. No metal solubility was found in the UO_2 pellet. Then nine different phases were found in the solidified liquid region.

Five different borides that do not contain uranium were identified:

- (Cr, Fe)B – with a dendritic shape. It suggests that this is the first phase to form during solidification. EPMA provided accurate composition measurements underlining a large amount of Cr. It diffracts in EBSD as Cmcm space group and CrB-type structure (Pearson Symbol: *oC*8) contrary to the (Fe,Cr)B phase measured in sample n°1 with Pnma FeB-type structure;
- $(Fe, Cr, Ni)_2B$ – diffracting with a I4/mcm space group and Al_2Cu-type (Pearson symbol:*tI*12). This phase solidified in a rectangular shape, as shown in Figure 4;
- $(Fe, Cr, Ni)_2B$ – diffracting with Fddd space group and Mg_2Cu-type (Pearson symbol: *oF*24). EBSD allowed differentiating two $(Fe, Cr, Ni)_2B$ phases with tI12 and oF24 structures, respectively. Both $(Fe, Cr, Ni)_2B$ grain compositions are close and cannot be distinguished in BSE micrographs. EPMA showed slight differences in Fe and Cr concentrations with a higher Cr-content in the *oF*24. The phase with *tI*12 structure has minor proportion in the sample. The (Cr,Fe)B phase is always surrounded by $(Fe,Cr,Ni)_2B$ precipitates. This microstructure shows that during solidification the (Cr,Fe)B phase may act as preferential nucleation site for $(Fe,Cr,Ni)_2B$ phases ;
- $(Cr,Fe,Ni,Mo,Ti)_3B_2$ – this phase appears in the shape of rectangular and triangular precipitates. It diffracts with P4/mbm space group and U_3Si_2-type (Pearson symbol *tP*10) ;

- Small local precipitates of (Ti,Fe,Mo,Cr)B_2 were found using EDS analysis.

Five phases containing uranium were found in the solidified liquid. Each crystallographic structure could not be clearly identified:

- The region labelled as “matrix” in Figure 4b and Figure 4c contains two phases impossible to distinguish in BSE image. This matrix hosts most of the metallic U and Ni. Both phases have the same U content (about 14 at%). Figure 5 displays the matrix overall composition as function of distance from the pellet and show the presence of a metallic and a boride phase in the matrix. These phases are assumed to be uranium mixed boride U(Fe,Ni)$_4$B (labelled UM_4B in Figure 5) and a metallic phase U(Fe,Ni)$_5$ according EPMA quantification. The results from EBSD analysis remain unclear. A part of the matrix region diffracts with *fcc* structure. The identification of both phases relies on the EPMA results and similarities with sample n°3 analysis. Eutectic microstructures are visible within the matrix. It shows that the matrix remained in the liquid state until the total solidification of the sample.

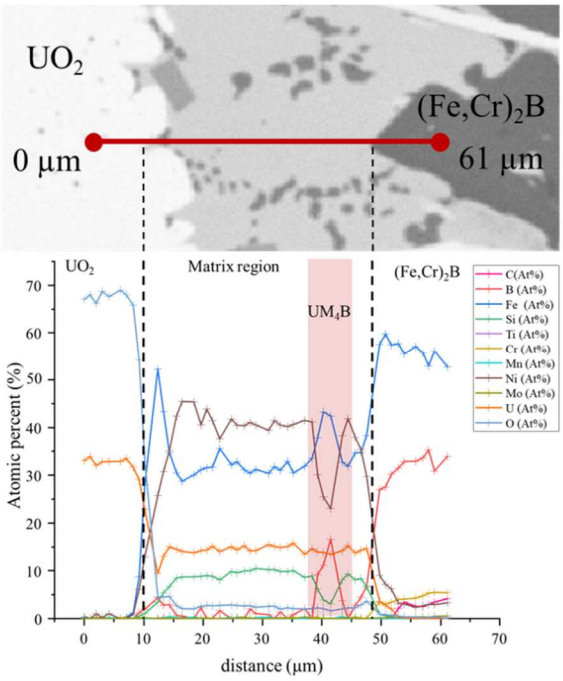

Figure 5 Composition profile measurement near the UO_2 pellet interface. At the top is a BSE image where the composition profile was performed. At the bottom is the chemical composition profile in atomic percent as a function of the distance; dash lines delimit the matrix region, the red area labelled as UM_4B corresponds to the $U(Fe,Ni)_4B$ phase. The metallic region is assumed as $U(Ni,Fe)_5$.

- A needle-shaped phase with high chemical contrast implying a high U-content is visible among the solidified liquid microstructure. The small size of these precipitates in addition to the unclear diffraction results make its clear identification challenging.
- UFe_3B_2 – diffracting with P6/mmm space group, $CeCo_3B_2$-type (Pearson symbol: *hP*6). Only traces in EBSD map were observed. No EPMA data can support the identification of the phase;
- (U,Y) $O_{2\pm x}$ oxide diffracting with *fcc* structure. Y coming from the Y_2O_3 crucible was measured only in UO_2 grains taken off from the pellet due to the intergranular penetration of the liquid in the UO_2 pellet. It underlines that a slight interaction occurred with the crucible.

These experimental results show that most of boride phases formed during the solidification are Fe and Cr based as already observed in previous works [11,14,24]. Only the boride $U(Fe,Ni)_4B$ phase contains a significant amount of Ni and U. As Ni and U have the tendency to form numerous compounds, Ni is also found in the intermetallic compound $U(Ni,Fe)_5$ in which Fe is dissolved.

In comparison with sample n°1, a significant amount of uranium coming from the UO_2 pellet dissolution into the liquid was found. Also, carbon was found as trace in the sample, which means that it was consumed during the heat treatment.

EPMA measurements performed in random matrix spot show the U proportion is not correlated with the distance to the pellet (supplementary materials). No composition gradient occurs and the uranium is homogeneously distributed in the liquid phase. Both the uniform grains distribution as well as the consistent U content suggest that the annealing dwell of one hour was long enough to reach the equilibrium composition.

3.3.Sample n°3

The sample contains a larger amount of UO_2 than sample n°2. As for sample n°2, the experimental conditions lead to a (liquid + UO_2) equilibrium. A uniform wetting and an intergranular penetration of the liquid at the UO_2 grain boundaries are observed, similarly to sample n°2. The results using EDS, EPMA and EBSD are consistent for most of the phases. Overall EPMA measurement shows U occurrence in the solidified liquid phase region. No significant amount of C is detected (Table 4). Phases compositions are reported in Table 5, and BSE micrographs and EBSD phase map are presented in Figure 6.

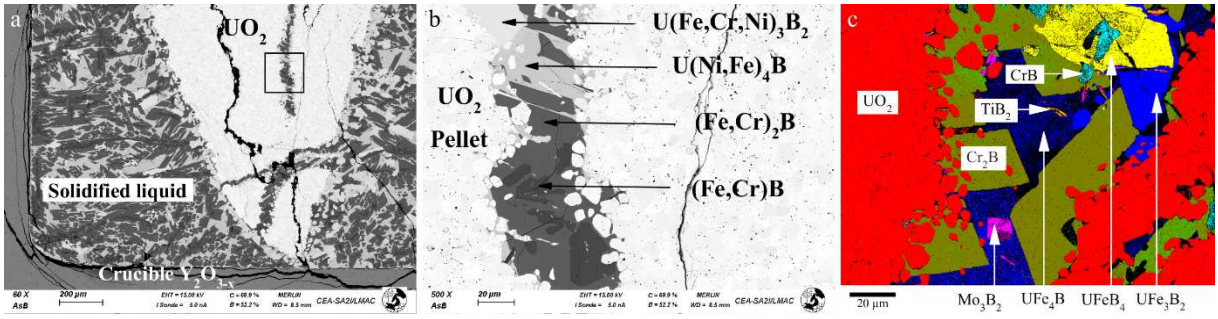

Figure 6 BSE image of sample n°3 – a) zoom x60, black square indicates the location of the image b) – b) Zoom x500 – c) EBSD structure map zoom x700, legend corresponds to the indexed structure as compound-like notation

Twelve phases are found in the sample, including UO_2 as remaining pellet chip. Eleven phases are analysed in the solidified liquid region:

- (Cr, Fe)B – diffracting with Cmcm space group and CrB-type. It has a dendritic shape and is always surrounded by (Fe, Cr, Ni)$_2$B;
- (Fe, Cr, Ni)$_2$B – diffracting with a I4/mcm space group and Al_2Cu-type (Pearson symbol:*tI*12), the precipitates adopt a large rectangular shape;
- (Mo,Fe,Cr,Ni,Ti)$_3$B$_2$ – as small rectangular and triangular shape precipitates. It diffracts with P4/mbm space group and U3Si2-type (Pearson symbol *tP*10);
- (Ti,Mo)B$_2$ – diffracting with P6/mmm space group, AlB_2-type (Pearson symbol: *hP*3);
- U(Fe,Cr)B$_4$ – diffracting with Pbam space group, $YCrB_4$-type (Pearson symbol: *oP*28);
- U(Fe,Ni)$_3$B$_2$ – diffracting with P6/mmm space group, $CeCo_3B_2$-type (Pearson symbol: *hP*6);
- Precipitates with an acicular shape (similar than in sample n°2). The precipitate diffract with Cmcm space group, V_2B_3-type (Pearson symbol: *oS*20). Their occurrence is less important than in the sample n°2;
- U(Fe,Ni)$_4$B – diffracting with P6/mmm space group; UCo_4B – type (Pearson symbol: *hP*6);
- U$_6$(Fe,Ni)$_{23}$ – diffracting with Fm-3m space group; Th_6Mn_{23} – type (Pearson symbol: *cF*116);
- The assumed metallic compound U(Ni,Fe)$_5$ which could not be confirmed with EBSD;
- (U,Y)$O_{2\pm x}$ – diffracting as *fcc* in removed grains and along the interface with the crucible are also identified.

The microstructure and the phase compositions of sample n°3 are very similar to sample n°2, except for the formation of three extra phases: U(Fe,Cr)B$_4$, U(Fe,Ni)$_3$B$_2$ and U$_6$(Ni,Fe)$_{23}$. Cr tends to locate in B-rich phases (Cr, Fe)B, (Fe, Cr, Ni)$_2$B and U(Fe,Cr)B$_4$ while Ni preferentially locates in B-poor phases U(Fe,Ni)$_4$B, U$_6$(Fe,Ni)$_{23}$ and U(Ni,Fe)$_5$. EPMA

cartography presented in supplementary materials well depicted this behaviour. In both case the assumed $U(Fe,Ni)_5$ phase couldn't be identified with confidence because crystallographic structure remain unclear. Both samples show complex solidification behaviour involving U-Ni-Fe metal phases that do not correspond to the phases from the associated binary systems.

Table 4 Atomic composition of the solidified liquid through EPMA overall measurements. Average over 10 analyses covering squares areas of 200 µm width each.

(At%)	C	B	Fe	U	Si	Ti	Cr	Ni	Mo
Sample n°1	22.8	28.2	32.2	/	0.7	0.4	8.1	6.8	0.5
Sample n°2	/	26.0	46.8	3.0	0.8	0.3	11.9	10.0	0.5
Sample n°3	/	38.5	36.2	5.0	1.1	0.3	8.4	10.0	0.6

Table 5 Description of phases identified in solidified liquids for samples 1, 2 and 3. Identification relies on EPMA, EDS, and EBSD cross-measurements.

Sample	Structure-type and Pearson symbol	Phase identification	Chemical composition from EPMA (at%)	Phase identification from cross measurements
1	Al_2Cu – *tI*12	$(Fe,Cr,Ni)_2B$	52Fe-29B-8Cr-7Ni-4C	$(Fe_{0.77},Cr_{0.12},Ni_{0.11})_{2.1}(B_{0.89},C_{0.11})$
	FeB – *oP*8	(Fe,Cr)B	47B-27Fe-20Cr-2Ni-3C-1Mo	$(Fe_{0.55},Cr_{0.42},Ni_{0.03})(B_{0.95},C_{0.05})$
	fcc	Fe,Cr,Ni,Mo	37Fe-38Ni-8Si-8B-4C-2Cr-1Mn	/
2	Mg_2Cu – *oF*24	$(Fe,Cr,Ni)_2B$	44Fe-33B-17Cr-3Ni-3C	$(Fe_{0.71},Cr_{0.24},Ni_{0.04})_{1.8}(B_{0.93},C_{0.07})$
	Al_2Cu – *tI*12	$(Fe,Cr,Ni)_2B$	52Fe-32B-8Cr-4Ni-4C	$(Fe_{0.81},Cr_{0.13},Ni_{0.06})_{1.83}(B_{0.90},C_{0.10})$
	CrB – *oC*8	(Cr,Fe)B	49B-32Cr-14Fe-2C-1Mo	$(Cr_{0.66},Fe_{0.29},Mo_{0.03})(B_{0.96},C_{0.04})$
	No EBSD data	$U(Fe,Ni)_5$	39Ni-33Fe-14U-9Si-2O-2B	/
	UCo_4B – *hP*6	$U(Fe,Ni)_4B$	40Fe-29Ni-14U-12B-3Si-2O	$U(Fe_{0.55},Ni_{0.40},Si_{0.05})_{5.23}(B_{0.87},O_{0.13})_{1.01}$
	U_3Si_2 – *tP*10	$(Fe,Mo,Cr,Ni,Ti)_3B_2$	36B-25Fe-14Mo-7Cr-6Ni-4Ti-3W-2C-1U	$(Fe_{0.40},Mo_{0.22},Cr_{0.12},Ni_{0.09},Ti_{0.07}W_{0.05})_3(B_{0.95},C_{0.05})_{1.94}$
	$CeCo_3B_2$ – *hP*6	$U(Fe,Ni)_3B_2$	*No EPMA data*	/
	fcc	$(U,Y)O_{2\pm x}$	64O-18U-17Y	$(U_{0.51},Y_{0.49})O_{1.77}$
	AlB_2 – *hP*3	$(Ti,Fe,Mo,Cr)B_2$	*No EPMA data*	/
3	Al_2Cu – *tI*12	$(Fe,Cr,Ni)_2B$	51Fe-33B-14Cr-3Ni	$(Fe_{0.75},Cr_{0.20},Ni_{0.04})_{2.06}B$
	CrB – *oC*8	(Fe,Cr)B	50B-34Cr-14Fe-1Mo	$(Cr_{0.69},Fe_{0.28},Mo_{0.03})_{1.01}B$
	$CeCo_3B_2$ – *hP*6	$U(Fe,Ni)_3B_2$	*No EPMA data*	/
	U_3Si_2 – *tP*10	$(Mo,Fe,Cr,Ni,Ti)_3B_2$	39B-28Fe-24Mo-4Cr-3Ti-2Ni	$(Fe_{0.46},Mo_{0.39},Cr_{0.07},Ti_{0.06},Ni_{0.03})_{3.17}B_2$
	AlB_2 – *hP*3	$(Ti,Mo)B_2$	63B-23Ti-6Mo-4Cr-3Fe-1Ni	$(Ti_{0.64},Mo_{0.18},Cr_{0.10}, Fe_{0.07},Ni_{0.01})_{1.16}B_2$
	$YCrB_4$ – *oP*28	$U(Fe,Cr)B_4$	60B-20U-15Fe-4Cr	$U(Fe_{0.78},Cr_{0.22})_{1.02}B_{3.07}$
	UCo_4B – *hP*6	$U(Fe,Ni)_4B$	38Fe-31Ni-16B-15U	$U(Fe_{0.55},Ni_{0.45})_{4.67}B_{1.09}$

Th_6Mn_{23} – *cF*116	$U_6(Fe,Ni)_{23}$	60Ni-20U-20Fe	$U_6(Ni_{0.76},Fe_{0.24})_{23.75}$
V_2B_3 - *oS*20	/	/	/
No EBSD data	$U(Fe,Ni)_5$	52Ni-31Fe-16U-1Cr	$U(Fe_{0.37},Ni_{0.63})_{5.29}$
fcc	$(U,Y)O_{2-x}$	/	/

4. Discussion

The experimental results on samples n°2 and n°3 show the consumption of carbon and the dissolution of uranium in the liquid which are consistent with the following carbo-reduction reaction occurring at high temperature [25]: $UO_2 + 2\ C = 2\ CO + U$

In this reaction, carbon from B_4C reduces UO_2 to UO_{2-x} then to metallic U and induces the formation of gaseous CO. Similarly, Gosse et al. [26] and Plevacova et al. [17] observed the carbo-reduction reaction by mixing powder of UO_2 with B_4C. The reaction leaded to the formation of UB_4 at similar temperatures. The present work suggests that the carbo-reduction reaction also happened in presence of liquid SS. B from B_4C, which is dissolved in the SS liquid phase, may decrease the liquid surface tension and thus promote the wetting at the UO_2 interface. Metallic U should then be dissolved in the SS liquid while CO should leave the UO_2/liquid interface by vaporization. Kleykamp et al. [27] showed that uranium dissolution from UO_2 in liquid stainless steel at 2000°C remains very low in the UO_2-SS system. In our study, the presence of B_4C that enables carbo-reduction to occur is a key factor toward uranium dioxide reduction, which promotes the formation of metallic liquid phase. Gosse et al. [26] and Plevacova et al. [17] also measured the release of gaseous boron oxides species such as B_2O_3, B_2O_2 or BO during the carbo-reduction reaction. In our work, no trace of boron oxides was found in the samples or on the surface of the crucibles. High Temperature Mass Spectrometry measurements could be further performed to identify the gaseous species released from the sample.

Since the crucible is not sealed, CO(g) is released in the furnace vessel that induces the irreversible change in the sample composition. The mass loss measured after the heat

treatment for samples n°2 and n°3 are 18.5 mg and 14.5 mg, respectively. Considering a total carbo-reduction reaction, and UO_2 being in large excess, the theoretical mass of released CO(g) would be 16.78 mg for sample n°2 and 18.40 mg for sample n°3. The measured mass losses are consistent with the total carbo-reduction reaction. Traces of C were measured in the solidified liquid region as global C content is negligible. The reaction leads to the total consumption of C. Because UO_2 is in large excess, C can be considered as the limiting reactant in the carbo-reduction process. According to several authors [25,28–30] who showed that the carbo-reduction occurs in several steps involving uranium carbides formation in the system UO_2-C, traces of C may solidify as uranium carbide if enough C is available. Uranium mixed carbides are relevant candidates for acicular phases observed in both sample n°2 and n°3. Indeed, Ghosh et al. [31] showed that uranium carbides $(U,Pu)_yC_x$ may precipitate as needle-shaped phase. Similarly, Chubb et al. and Jones et al. [32,33] described ternary compounds UMC_2 (where M is an element among Fe, Cr, Ni, Mo or W) with orthorhombic space group having an acicular microstructure. The hypothesis of the total C reaction still applies, as acicular phase formation should result of C traces.

Thermodynamic calculations were performed to compute the phases in equilibrium at 1900°C. Taking the initial composition of sample n°2 and n°3 in Table 2, solid UO_2, liquid and gas are in equilibrium at 1900°C. The equilibrium pressures calculated at 1900°C are equal to 5.06 bar and 4.18 bar for samples n°2 and n°3, respectively. Table 6 presents the calculated composition of the gas in equilibrium with UO_2 and liquid at 1900°C using the TAF-ID database [16]. The Table 7 gives the calculated molar fraction of the phases at equilibrium pressures and 1900°C. We assume that the gas composition at equilibrium pressure is representative for the gas formed during the reaction. However, the crucible is not fully tight so some gas shall escape from the crucible and the pressure is probably not maintained during the heat-treatment.

Table 6 Calculated gas composition (at%) at 1900°C at equilibrium pressure of 5.06 bar and 4.18 bar for sample n°2 and n°3, respectively – CO content and secondary species are displayed in the table.

	Main specie	Secondary species			
Sample n°2	99.93% CO	0.02% B_2O_2	0.01% SiO	0.01% Fe	0.01% BO
Sample n°3	99.93% CO	0.02% B_2O_2	0.01% SiO	0.01% Fe	0.01% BO

Table 7 Calculated molar fractions of the phases in equilibrium at 1900°C and at equilibrium pressures (5.06 bar and 4.18 bar for sample n°2 and n°3, respectively)

	Calculated molar fraction of phases (at%)				
Phases at equilibrium	gas	liquid	$UO_{1.96}$	TiC	C graphite
Sample n°2	0.00%	79.70%	19.04%	0.51%	0.75%
Sample n°3	0.00%	71.21%	27.69%	0.47%	0.64%

The major species in the gas is CO (>99%at). The gas also contains small amounts of other oxides and metallic gaseous species. During the heat treatment, the continuous gas release drives the system toward an equilibrium between liquid and solid where C and O are removed in regard with CO formation. In order to demonstrate this carbo-reduction reaction, the experimental compositions of the solidified liquid region of samples n°2 and 3 are compared to the calculated ones after total CO(g) release in Figure 7. The conditions used for the calculations consider masses of initial components introduced in the sample in which the amount of released CO(g) is subtracted. Only the elements (Fe, Cr, Ni, B, U, O, Mo, Si and Ti) are considered. Supplementary materials specify input compositions and calculations values.

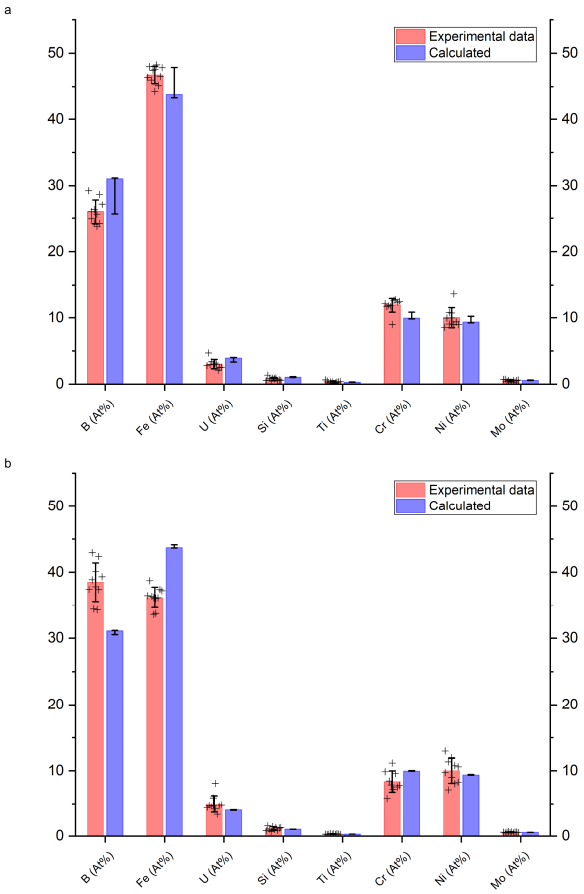

Figure 7 Comparison of liquid composition (at%) between EPMA analysis (red) and thermodynamic calculation (blue) for sample n°2 (a) and n°3 (b). Black crosses are the experimental compositions in atomic percent measured by EPMA within 200 µm large square areas, error bar is the associated standard deviation. Calculated errors are limit values considering mass losses during sample making.

The calculated composition of the liquid phase at 1900 °C is in good agreement with the overall composition of the solidified liquid phase measured by EPMA for both samples. This result reinforces the assumption of a reaction leaded by a carbo-reduction process and confirms that the experimental conditions allowed approaching thermodynamic equilibrium at 1900°C. Error bars are displayed in the calculated results to visualise the actual range of the

liquid phase composition taking into account synthesis mass losses. They are determined by performing boundary calculations considering that the loss was only B_4C or only SS.

5. Conclusion

Experimental investigation on the UO_2-B_4C-SS system highlights a carbo-reduction process at laboratory scale. The experiment showed the carbo-reduction between B_4C and UO_2 occurs in presence of SS. This reaction – $UO_2 + 2\ C = 2\ CO + U$ – induces UO_2 reduction into U which dissolves in the metallic liquid. In addition, C is fully consumed to form mainly gaseous CO. Experimental conditions ensure reliable mixing and good contact between solid and liquid phases at 1900°C. The experiment on UO_2-B_4C-SS samples also showed that one hour at 1900°C enables reaching thermodynamic equilibrium. Thus, thermodynamics calculations at high temperature are consistent with the experimental observations and may serve as a powerful tool in the description of the thermodynamic behaviour in severe accident conditions. Reaction mechanisms are still unknown and may vary with temperature. The investigation of the kinetic aspect of the reaction should lead to better understanding carbo-reduction mechanisms.

Because U partially dissolves in liquid at 1900°C, uranium boride phases form at solidification. Mixed uranium boride phase such as $U(Fe,Ni)_3B_2$, $U(Fe,Cr)_4B$ and $U(Fe,Cr)B_4$ were identified after solidification. The solidified liquid is mainly composed of borides $(Fe,Cr)_xB$. Ni preferentially solidifies in B-poor and U-rich intermetallic phases. Solidified liquid analysis gives reliable insights in the thermodynamic of the complex system UO_2-SS-B_4C. Results may serve enhancing performances in thermodynamic modelling of core materials.

In the scope of accident mitigation, the formation of chemical bonds between U and B during severe accident may have a positive impact on reactivity and may influence mitigation process.

The present experimental investigation showed that Fe-Cr-B, U-Fe-B and U-Fe-Ni ternary systems are the key ternary systems to describe the behaviour of the liquid during solidification. Specific investigations about those systems might enhance understanding of core materials behaviour in SFR reactor.

Investigation were performed over UO_2 as fuel material instead of MOx. As Pu content influences the oxygen potential of fuel, it may affect the carbo-reduction process. From this statement, we expect higher tolerance to hypo-stoichiometry in MOx. Therefore, everything else equal, carbo-reduction of MOx should limit fuel elements dissolution into liquid phase compare to UO_2. Future research should consider experimenting the effect of Pu content in the carbo-reduction.

6. Credit authorship contribution statement

Mathieu Garrigue[a]: Visualization, Conceptualization, Formal analysis, Investigation, Methodology, Writing - original draft.

Andrea Quaini[a*]: Supervision, Conceptualization, Validation, Methodology, Writing – review & editing

Thiery Alpettaz[a] : Investigation

Christophe Bonnet[a] : Investigation

Emmanuelle Brackx[b]: Investigation, Writing – review & editing

Renaud Domenger[b]: Investigation

Matthieu Touzin[c]: Investigation, Writing – review & editing

Olivier Tougait[d]: Investigation, Writing – review & editing

Christine Guéneau[a]: Supervision, Validation, Writing – review & editing.

7. Declaration of interest statement

The authors declare that they have no known competing financial interests or personal relationships that could have appeared to influence the work reported in this paper.

8. Acknowledgment

The authors would like to thank the Generation IV reactor program of the industrial nuclear support and innovation Division of CEA which supports this work as well as the SFR R&D Project. The SEM and EPMA facilities in Lille (France) are supported by the Conseil Régional des Hauts de France and the European Regional Development Fund (ERDF). S. Bellayer is warmly thanked for her precious contribution in the EPMA analyses in Lille.

9. References

[1] W. Maschek, A. Rineiski, M. Flad, P. Liu, X.N. Chen, Y. Tobita, H. Yamano, T. Suzuki, S. Fujita, K. Kamiyama, S. Pigny, T. Cadiou, K. Morita, G. Bandini, The SIMMER safety code system and its validation efforts for fast reactor application, International Conference on the Physics of Reactors 2008, PHYSOR 08. (2008) 2370–2378.

[2] F. Bertrand, N. Marie, G. Prulhière, J. Lecerf, J.M. Seiler, Comparison of the behaviour of two core designs for ASTRID in case of severe accidents, Nuclear Engineering and Design. 297 (2016) 327–342. https://doi.org/10.1016/j.nucengdes.2015.04.020.

[3] P. Galon, V. Faucher, F. Casadeï, S. Potapov, Modelling complex fluid-structure interaction problems with EUROPLEXUS fast dynamic software, (2008) 17. https://doi.org/10.13140/RG.2.1.3402.1287.

[4] T. Beck, N. Chapoutier, J.-M. Escleine, L. Gauthier, D. Occhipinti, B. Perrin, C. Venard, Conceptual design of ASTRID radial shielding sub-assemblies, Nuclear Engineering and Design. 330 (2018) 129–137. https://doi.org/10.1016/j.nucengdes.2018.01.040.

[5] J. Papin, Behavior of Fast Reactor Fuel During Transient and Accident Conditions, in: Comprehensive Nuclear Materials, Elsevier, 2012: pp. 609–634. https://doi.org/10.1016/B978-0-08-056033-5.00047-1.

[6] S. Poumerouly, Neutronics aspects associated to the prevention and mitigation of severe accidents in sodium cooled reactor cores, Institut Polytechnique de Grenoble Univ., 2010. http://inis.iaea.org/Search/search.aspx?orig_q=RN:43035127 (accessed August 2, 2021).

[7] J. Charpenel, F. Lemoine, I. Sato, D. Struwe, W. Pfrang, Fuel Pin Behavior under the Slow Power Ramp Transients in the CABRI-2 Experiments, Nuclear Technology. 130 (2000) 252–271. https://doi.org/10.13182/NT00-A3092.

[8] Z. Chen, X.-N. Chen, A. Rineiski, P. Zhao, H. Chen, Coupling a CFD code with neutron kinetics and pin thermal models for nuclear reactor safety analyses, Annals of Nuclear Energy. 83 (2015) 41–49. https://doi.org/10.1016/j.anucene.2015.03.023.
[9] S. Poumerouly, Neutronics aspects associated to the prevention and mitigation of severe accidents in sodium cooled reactor cores, (2010). http://inis.iaea.org/Search/search.aspx?orig_q=RN:43035127 (accessed July 24, 2019).
[10] G. Kayser, J. Charpenel, C. Jamond, Summary of the SCARABEE-N Subassembly Melting and Propagation Tests with an Application to a Hypothetical Total Instantaneous Blockage in a Reactor, Nuclear Science and Engineering. 128 (1998) 144–185. https://doi.org/10.13182/NSE98-A1950.
[11] P. Hofmann, M.E. Markiewicz, J.L. Spino, Reaction behavior of B4C absorber material with stainless steel and zircaloy in severe light water reactor accidents, Nuclear Technology. 90 (1990) 226–244. https://doi.org/10.13182/NT90-A34417.
[12] H. Shibata, K. Sakamoto, A. Ouchi, M. Kurata, Chemical interaction between granular B_4C and 304L-type stainless steel materials used in BWRs in Japan, Journal of Nuclear Science and Technology. 52 (2015) 1313–1317. https://doi.org/10.1080/00223131.2015.1011721.
[13] S. Sao Joao, C. Duriez, C. Dominguez, D. Jacquemain, Light elements microanalysis of steel/B4C melts for nuclear power plants accident studies, Microchimica Acta. 161 (2008) 343–348. https://doi.org/10.1007/s00604-007-0855-3.
[14] M.S. Veshchunov, P. Hofmann, Modelling of the interactions between B4C and stainless steel at high temperatures, Journal of Nuclear Materials. 226 (1995) 72–91. https://doi.org/10.1016/0022-3115(95)00094-1.
[15] T. Sumita, T. Kitagaki, M. Takano, A. Ikeda-Ohno, Solidification and re-melting mechanisms of SUS-B4C eutectic mixture, Journal of Nuclear Materials. 543 (2021) 152527. https://doi.org/10.1016/j.jnucmat.2020.152527.
[16] C. Guéneau, N. Dupin, L. Kjellqvist, E. Geiger, M. Kurata, S. Gossé, E. Corcoran, A. Quaini, R. Hania, A.L. Smith, M.H.A. Piro, T. Besmann, P.E.A. Turchi, J.C. Dumas, M.J. Welland, T. Ogata, B.O. Lee, J.R. Kennedy, C. Adkins, M. Bankhead, D. Costa, TAF-ID: An international thermodynamic database for nuclear fuels applications, Calphad. 72 (2021) 102212. https://doi.org/10.1016/j.calphad.2020.102212.
[17] K. Plevacova, Etude des matériaux sacrificiels absorbants et diluants pour le contrôle de la réactivité dans le cas d'un accident hypothètique de fusion du coeur de réacteurs de quatrième génération., Orléans, 2010.
[18] T. Beck, V. Blanc, N. Chapoutier, J.M. Escleine, L. Gauthier, D. Haubensack, D. Occhipinti, M. Pelletier, M. Phelip, B. Perrin, C. Venard, Conceptual design of fuel and radial shielding sub-assemblies for ASTRID, in: AIEA International Conference on Fast Reactors and Related Fuel Cycles (IAEA-FR17), Yekaterinburg, Russia, 2017. https://hal-cea.archives-ouvertes.fr/cea-02435081 (accessed June 17, 2020).
[19] A. Quaini, C. Guéneau, S. Gossé, N. Dupin, B. Sundman, E. Brackx, R. Domenger, M. Kurata, F. Hodaj, Contribution to the thermodynamic description of the corium – The U-Zr-O system, Journal of Nuclear Materials. 501 (2018) 104–131. https://doi.org/10.1016/j.jnucmat.2018.01.023.
[20] P. Nikolopoulos, E. Nold, H. Schneider, B. Schulz, The influence of sodium vapour on the wetting of UO2-stainless steel 1.4970 (liquid) and its interpretation using scanning auger spectroscopy, Journal of Nuclear Materials. 101 (1981) 277–287. https://doi.org/10.1016/0022-3115(81)90170-7.
[21] P. Nikolopoulos, G. Ondracek, Interfacial energies between uraniumdioxide and liquid metals, Journal of Nuclear Materials. 98 (1981) 306–312. https://doi.org/10.1016/0022-3115(81)90156-2.

[22] M. Takano, T. Nishi, N. Shirasu, Characterization of solidified melt among materials of UO2 fuel and B4C control blade, Journal of Nuclear Science and Technology. 51 (2014) 859–875. https://doi.org/10.1080/00223131.2014.912567.
[23] M. Aizenshtein, I. Mizrahi, N. Froumin, S. Hayun, M.P. Dariel, N. Frage, Interface interaction in the B4C/(Fe–B–C) system, Materials Science and Engineering: A. 495 (2008) 70–74. https://doi.org/10.1016/j.msea.2007.06.100.
[24] F. Nagase, H. Uetsuka, T. Otomo, Chemical interactions between B4C and stainless steel at hightemperatures, Journal of Nuclear Materials. 245 (1997) 52–59. https://doi.org/10.1016/S0022-3115(96)00747-7.
[25] S. Gossé, C. Guéneau, T. Alpettaz, S. Chatain, C. Chatillon, F. Le Guyadec, Kinetic study of the UO2/C interaction by high-temperature mass spectrometry, Nuclear Engineering and Design. 238 (2008) 2866–2876. https://doi.org/10.1016/j.nucengdes.2008.01.019.
[26] S. Gossé, T. Alpettaz, C. Guéneau, P. Allegri, High Temperature Thermochemistry of (U-Pu)O_2 MOX Fuel with B_4C absorber: Application to severe accidents in SFR, in: Fast Reactors and Related Fuel Cycles: Safe Technologies and Sustainable Scenarios (FR13). COMPANION CD-ROM. Proceedings of an International Conference, International Atomic Energy Agency (IAEA), Monti, S. (ed.); International Atomic Energy Agency, Department of Nuclear Energy, Vienna (Austria), 2015: p. 10. http://wwwpub. iaea.org/MTCD/Publications/PDF/SupplementaryMaterials/P1665CD/Track3_Safety.pdf (accessed June 5, 2019).
[27] H. Kleykamp, Phase equilibria in the UO2-austenitic steel system up to 3000°C, Journal of Nuclear Materials. 247 (1997) 103–107. https://doi.org/10.1016/S0022-3115(97)00033-0.
[28] S.K. Mukerjee, J.V. Dehadraya, V.N. Vaidya, D.D. Sood, Kinetic study of the carbothermic synthesis of uranium monocarbide microspheres, Journal of Nuclear Materials. 172 (1990) 37–46. https://doi.org/10.1016/0022-3115(90)90007-A.
[29] S.K. Mukerjee, J.V. Dehadraya, V.N. Vaidya, D.D. Sood, Kinetics and mechanism of UO2 + C reaction for UCUC2 preparation, Journal of Nuclear Materials. 210 (1994) 107–114. https://doi.org/10.1016/0022-3115(94)90228-3.
[30] H. Wilhelm, The carbon reduction of uranium oxide, Ames Laboratory Technical Reports. (1964). https://lib.dr.iastate.edu/ameslab_isreports/86.
[31] J.K. Ghosh, D. Vollath, Metallography of Uranium Carbides and Uranium-Plutonium-Mixed Carbides, (1974). https://doi.org/10.5445/IR/270007431.
[32] W. Chubb, D.L. Keller, Constitution of the systems of uranium and carbon with molybdenum, niobium, rhenium, tungsten, and yttrium, 1964. https://doi.org/10.2172/4018761.
[33] D.W. Jones, I.J. McColm, J. Yerkess, N.J. Clark, Carbon species in the crystal structures of uranium-transition-element carbides,UMC2, Journal of Solid State Chemistry. 74 (1988) 304–313. https://doi.org/10.1016/0022-4596(88)90359-3.